Unstructured Overset Mesh Adaptation with Turbulence Modeling for Unsteady Aerodynamic Interactions

Rajiv Shenoy* and Marilyn J. Smith†
Georgia Institute of Technology, Atlanta, Georgia 30332
and
Michael A. Park‡
NASA Langley Research Center, Hampton, Virginia 23681

Schemes for anisotropic grid adaptation for dynamic overset simulations are presented. These approaches permit adaptation over a periodic time window in a dynamic flowfield so that an accurate evolution of the unsteady wake may be obtained, as demonstrated on an unstructured flow solver. Unlike prior adaptive schemes, this approach permits grid adaptation to occur seamlessly across any number of grids that are overset, excluding only the boundary layer to avoid surface manipulations. A demonstration on a rotor/fuselage-interaction configuration includes correlations with time-averaged and instantaneous fuselage pressures, and wake trajectories. Additionally, the effects of modeling the flow as inviscid and turbulent are reported. The ability of the methodology to improve these predictions is confirmed, including a vortex/fuselage-impingement phenomenon that has before now not been captured by computational simulations. The adapted solutions exhibit dependency based on the choice of the feature to form the adaptation indicator, indicating that there is no single best practice for feature-based adaptation across the spectrum of rotorcraft applications.

Nomenclature

C	=	coarsening factor
C_T	=	thrust coefficient, $T/(\rho\pi R^2(\Omega R)^2)$
c	=	rotor blade chord, m
c_p	=	pressure coefficient
$F_{e,(-)}$	=	adaptation formulation across an edge based on a solution feature
F_{tol}	=	user-specified adaptation tolerance
$f_{\bar{c}_p}$	=	time-averaged fuselage-centerline pressure integral
H	=	Hessian matrix
h^0	=	original mesh spacing, grid units
h_1	=	new mesh-spacing request, grid units
$\hat{I}$	=	adaptation intensity
k_{sgs}	=	subgrid-scale turbulence kinetic energy
l_e	=	edge length, grid units
M	=	anisotropic adaptation metric
N	=	number of time steps within adaptation window
n	=	time-step index within adaptation window
n_1, n_2	=	node (1 or 2) of given edge
p	=	static pressure, N/m²
R	=	rotor radius, m
Re_c	=	Reynolds number based on blade chord and tip speed, $V_{tip}c/\nu$
S	=	strain-rate tensor, s⁻¹
T	=	rotor thrust, N
V_{tip}	=	rotor tip speed, m/s
w	=	adaptation time window
x	=	streamwise direction, m
z	=	vertical direction, m
β_{1s}, β_{1c}	=	lateral and longitudinal first flapping harmonics, deg
μ	=	rotor advance ratio
μ_t	=	eddy viscosity
ν	=	kinematic viscosity, m²/s
ρ	=	density, kg/m³
ψ	=	blade azimuth angle, deg
Ω	=	rotation-rate tensor, s⁻¹
$|\omega|$	=	vorticity magnitude, s⁻¹

I. Introduction

THE resolution of unsteady wake features is essential for a multitude of unsteady aerodynamic and aeroelastic applications pertinent to rotorcraft. These include, but are not limited to, modeling of aeroelastic rotor blades in forward flight, rotor–fuselage (RFI) or rotor–rotor interaction, helicopter–ship interaction, tail wag, and tail buffet. Other applications of interest can include wing store separation, ship-wake interactions, and wind turbines. The current computational fluid dynamics (CFD) approach to resolve these multiple reference-frame applications is via overset grids, in which the moving body or component meshes are generally highly refined and overset on one or more static background grids [1–5]. Despite the ability of unstructured overset methods to model dynamic bodies, this approach does not address the issue of numerical dissipation that can result in inaccuracy of the wake physics [5,6].

Feature-based grid adaptation for unsteady problems has been applied on non-overset grids using various methodologies. Accurate predictions of hovering rotors in a single rotating adaptive mesh have been performed by several researchers [7–10]. However, these scenarios cannot be immediately applied to the prediction of rotors in forward flight, in which adaptation is needed in both the background inertial reference frame and the near-body rotating frame. Further, the interaction of rotors with nonmoving bodies such as fuselages, wind-tunnel struts, and other configurational components also requires moving-grid capability to simulate multiple motion frames. As an alternative to the overset configuration, Nam et al. [11] have demonstrated an unstructured sliding-mesh approach, in which a rotating grid communicates with a stationary background grid. Here, articulation of the rotor blades was made possible using grid deformation based on a spring analogy, along with feature-based grid adaptation. Another non-overset-based approach has been described

*Graduate Research Assistant, School of Aerospace Engineering, 270 Ferst Drive. Student Member AIAA.
†Associate Professor, School of Aerospace Engineering. Associate Fellow AIAA.
‡Research Scientist, Computational Aerosciences Branch, Mail Stop 128. Senior Member AIAA.

by Cavallo et al. [12], which uses unstructured grid movement and deformation to enable moving-body adaptation.

Past research efforts in overset adaptation have in many instances relied on an off-body (background) Cartesian-grid-based adaptive capability. Meakin [13] presented a grid component grouping algorithm with overset structured grids using a method of adaptive spatial partitioning and refinement, and applied it to background Cartesian grids. Variations of this technique have been subsequently demonstrated by Henshaw and Schwendeman [14] and Kannan and Wang [15]. Canonne et al. [16] used an overset structured cylindrical grid topology to simulate rotor motion in hover, in which the background grid is adapted. Hybrid-solver developmental efforts have focused on rotor methodologies, in which two separate solvers are applied in the near-body and background regions, respectively. Duque et al. [17] have employed a structured near-body and unstructured wake-grid approach to evaluate rotors. Here, isotropic adaptation was applied on the unstructured background grid operating in a noninertial reference frame. This work recommended the use of anisotropic adaptation to accurately capture inherently anisotropic phenomena such as tip vortices. Sankaran et al. [18] and Wissink et al. [19–21] have successfully implemented automatic mesh refinement in a Cartesian solver to resolve the wake based on flowfield features. This high-order Cartesian solver is coupled to a body-fitted unstructured solver to resolve complex geometries.

The effect of time dependency on the flowfield is an essential aspect in applying grid adaptation to study dynamic bodies. Researchers [12,16] have shown that adapting the solution at a given frequency (based on flow time) has proven effective, with increasing frequency yielding higher accuracy. Investigations involving off-body Cartesian-based adaptive mesh refinement [14,15,18–21] have extended this rationale to adapt the solution at a frequency comparable to that of the solver time step, allowing for a coupled adaptive flow solver. However, this capability is not computationally efficient for mixed-element unstructured methods, as they do not have the advantage of octree data structures to provide for the adaptive mechanics.

An alternative approach is thus required, which addresses the time-dependency issue without the computational overhead of frequent adaptation. Kang and Kwon [8] present an adaptation technique that detects the local maxima of a vortex core every 5 deg, and using a three-dimensional parabolic blended curve to represent the vortex-core path. Nam et al. [11] describe a quasi-unsteady adaptive procedure for rotors in forward flight based on a time period or window dependent on the blade-passing frequency. Cells satisfying an adaptation indicator are marked at each time step within the window, and adaptation is performed for those cells at the conclusion of each window. Jung and Kwon [22] extend this technique for unstructured overset grids using Euler calculations. The extension of a time-dependent feature-based adaptation methodology for anisotropic grids involving dynamic bodies is delineated by Alauzet and Olivier [23].

These successful implementations of grid adaptation provide impetus for further investigation of this approach for rotorcraft applications involving multiple grids. What is common across these prior overset-based efforts is that the adaptation is restricted to the off-body background meshes. Because vorticity originates on a viscous surface where the near-body grid is employed, the full capability of the adaptation cannot be exploited unless the adaptation can occur across the meshes.

This paper presents a new adaptation strategy that permits time-dependent anisotropic adaptation for dynamic overset Navier–Stokes simulations. Furthermore, the selection of the turbulence model with respect to solution accuracy is investigated. Because an unstructured background grid can encompass many complex stationary bodies (e.g., fuselage, nacelle, and tower), the overset grid-refinement complexity inherent in a structured grid-based approach is avoided. The current development dictates adaptation to be executed over a periodic time window in a dynamic flowfield, so that an accurate evolution of the unsteady wake may be obtained using one unstructured flow solver.

II. Methodology

A. Flow Solver

FUN3D, an unstructured Reynolds-averaged Navier–Stokes (RANS) solver developed at NASA, was selected as the flow solver with which to demonstrate the new adaptation strategy. FUN3D uses an implicit node-based finite volume scheme to resolve the RANS equations on unstructured mixed-topology grids [24]. Both compressible and incompressible [25] Mach-regime capabilities are available in the flow solver. Time accuracy is achieved using a second-order backward differentiation formula (BDF2-opt) [26]. Roe's flux-difference splitting scheme [27] is used to compute the inviscid fluxes, whereas an equivalent central-difference approximation is used to resolve the viscous fluxes. A red–black relaxation scheme is used to solve the resulting linear system of equations. FUN3D has a plethora of turbulence methods available, of which Menter's $k\omega$-shear-stress transport (SST) [28] and the hybrid RANS–large-eddy simulation (HRLES) [29] models were applied in this effort. SUGGAR + + [30] and DiRTlib [31] provide overset capability with FUN3D, and have been successfully used for compressible and incompressible rotorcraft applications [3,5]. In such simulations, the background grid, which consists of the fuselage and other wind-tunnel static geometries up to the far-field boundaries, is assembled with near-body grids for each of the moving rotor blades.

B. Anisotropic Feature-Based Adaptation

FUN3D's anisotropic tetrahedral adaptation capability [32,33] formed the basis for the new adaptation strategy. This functionality has been applied to investigate several applications, such as sonic-boom propagation [34,35], viscous transonic drag prediction [34], and reentry-vehicle configurations [36]. Feature-based adaptation requires the identification of a feature or indicator, as well as a formulation to define the grid modification. In this effort, the indicators explored were vorticity, pressure-difference, and the Q-criterion. The vorticity adaptation formulation, $F_{e,|\omega|}$, is similar to the one applied by Duque et al. [17], which scales vorticity (ω) with an edge length l_e. For the given edge connecting nodes n_1 and n_2, the vorticity formulation is computed based on the averaged vorticity magnitude across the edge:

$$F_{e,|\omega|} = l_e \frac{|\omega|_{n_1} + |\omega|_{n_2}}{2} \qquad (1)$$

The pressure-difference formula, $F_{e,\Delta p}$, was defined as the magnitude of the pressure difference Δp over an edge scaled by the edge length l_e as

$$F_{e,\Delta p} = l_e |p_{n_1} - p_{n_2}| \qquad (2)$$

The formulation of the Q-criterion indicator is based on Kamkar's nondimensional method [37], and uses the rotation-rate Ω and strain-rate S tensors. Here, the maximum value across the edge is applied:

$$F_{e,Q\text{-crit.}} = \max_{n_1, n_2}\left[\frac{1}{2}\left(\frac{\|\Omega\|^2}{\|S\|^2} - 1\right)\right] \qquad (3)$$

Using either of these formulations, the normalized local adaptation intensity $\hat{I}$ is derived for each node as the maximum of the edge formulation F_e over all incident edges of a given node:

$$\hat{I} = \max_{\text{edges}}\left(\frac{F_e}{F_{\text{tol}}}\right) \qquad (4)$$

in which F_{tol} is a user-specified tolerance. The new isotropic mesh spacing is calculated using an estimate of the spacing on the original mesh h^0, a coarsening factor C (typically around 115%), and an adaptation intensity as

$$h_1 = h^0 \min\left[C, \left(\frac{1}{\hat{I}}\right)^{0.2}\right] \qquad (5)$$

The power of 0.2 is an underrelaxation parameter that controls the aggressiveness of the refinement process. This parameter relates the convergence rate of error to the grid spacing for adjoint-based adaptation. The value of 0.2 (or $1/5$) has been found sufficient because the convergence rates for adjoint-based adaptation are about $O(h^4) - O(h^5)$ [38]. Although there is no formal connection to the local error estimates, this value has been typically chosen as a sufficient under-relaxation parameter for feature-based adaptation [36].

Consequently, an anisotropic adaptation metric may be derived using a scalar quantity for the isotropic spacing, and a Hessian to stretch the resulting mesh. The Hessian of a quantity $(-)$ can be described as

$$ H = \begin{vmatrix} \dfrac{\partial^2(-)}{\partial x^2} & \dfrac{\partial^2(-)}{\partial x \partial y} & \dfrac{\partial^2(-)}{\partial x \partial z} \\ \dfrac{\partial^2(-)}{\partial x \partial y} & \dfrac{\partial^2(-)}{\partial y^2} & \dfrac{\partial^2(-)}{\partial y \partial z} \\ \dfrac{\partial^2(-)}{\partial x \partial z} & \dfrac{\partial^2(-)}{\partial y \partial z} & \dfrac{\partial^2(-)}{\partial z^2} \end{vmatrix} \tag{6} $$

The Hessian is computed and decomposed into eigenvalues and eigenvectors, which are then scaled so that the largest eigenvalue (tightest spacing) corresponds to the spacing requirement, h_1. The anisotropic adaptation metric M is formed by taking the absolute value of the eigenvalues of this matrix. Further details of the computation of the Hessian-based metric and its significance to the adaptation process are delineated by Park [32]. In this paper, the vorticity-based and Q-criterion-based methods invoke the vorticity-magnitude Hessian to determine anisotropy, whereas the pressure-difference adaptation uses the Mach-number Hessian, described by Bibb et al. [36].

C.   Extension to Overset Grids

The overset grid-adaptation capability does not restrict adaptation to any component grid. This enables each grid to evolve independently, and, in general, ensures for an orphan free composite grid. The current adaptation capability for viscous flows is restricted only to nodes beyond the boundary layer for this demonstration of overset applications. FUN3D applies an adaptation software module that applies the adaptation metric as well as handles all associated adaptive mechanics. Details of the parallelized adaptation mechanics, which include grid operations such as node insertion and removal by splitting or collapsing edges, edge and face swapping, and node smoothing, are given in Park [32]. The extension of this method to include overset adaptation requires communication with DiRTlib [31], the grid connectivity module, to assign a component mesh ID for each node in the composite mesh. The code performs adaptation over the entire composite-grid system by tracking the component mesh ID for all added nodes.

Because the overset assembly of the component meshes is handled by a library outside of the FUN3D framework (SUGGAR++) [30], a generalized global-index convention was requisite so that subsequent assembly of the adapted grid with its domain-connectivity information would be compatible with the solution information. This process is required to perform valid solution transfers between the unadapted and adapted grid systems. The convention requires both the flow solver and adaptation code to assign composite-grid global indexes by arranging nodes in contiguous fashion by mesh ID over the list of component meshes. Nodes added due to adaptation are initially assigned new global indexes by appending them to the current global-index list. Node removal results in unused global indexes, which is handled by a reverse global-index-shifting procedure. To satisfy the condition of contiguous mesh IDs, a new procedure was introduced to re-sort the global indexes of the adapted grid system. After adaptation, the component meshes are then saved, and the resultant domain-connectivity information is obtained by invoking SUGGAR + + for subsequent grid assembly.

D.   Time-Dependent Adaptation

Time-dependent adaptation is obtained using a methodology based on that developed by Alauzet and Olivier [23]. The anisotropic metric is computed for every grid node at a given time step, and is progressively accumulated over a selected time window, such that the strongest restrictive metric at each node is retained to form the time-dependent grid metric. The time-dependent metric is formed by collecting N solution samples within a time window w as given by
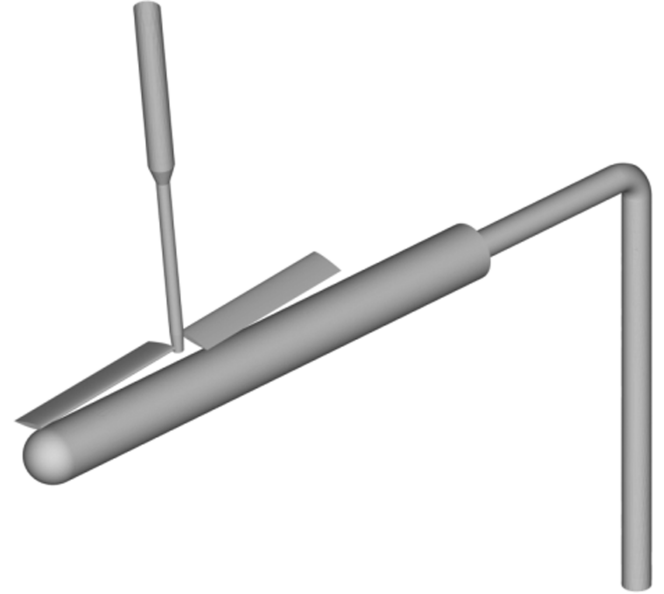
$$ |M_{w,\max}| = \bigcap_{n=1}^{N} |M_{w,n}| \tag{7} $$

Fig. 1   Model of the Georgia Institute of Technology RFI configuration.

a) $\psi = 240^\circ$ ($\psi = 60^\circ$)

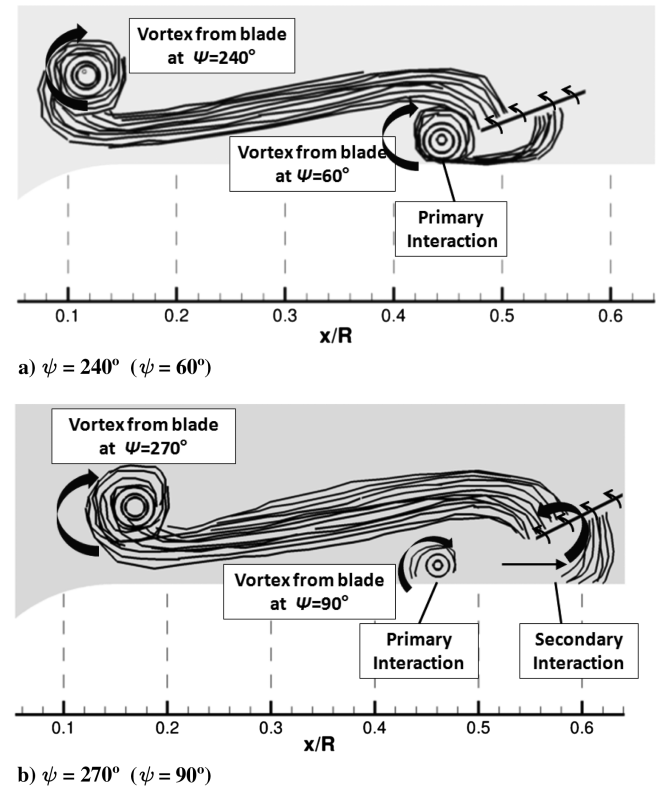b) $\psi = 270^\circ$ ($\psi = 90^\circ$)

Fig. 2   Approximate sketches of the vortex-fuselage interaction phenomena, adapted from Brand [39].

Using the resulting metric, a new adapted mesh may be obtained suitable for multiple time intervals characterized by the flow phenomena obtained within the adaptive window. For rigid-body rotorcraft simulations, such a window is identified as the time corresponding $1/n_{blades}$ revolutions. In this study, the solution is sampled at each time step throughout the time window to obtain the time-dependent metric. The present approach does not utilize a solution transfer capability; hence, no additional interpolation errors are introduced and the inherent solver accuracy is retained.

III. Georgia Institute of Technology Rotor/Fuselage-Interaction Configuration

A. Configuration Description

The Georgia Institute of Technology RFI configuration, as depicted in Fig. 1, comprises a cylindrical fuselage, and a hemispherical nose to permit general RFI analysis. This configuration has been extensively evaluated in the Haper wind tunnel [39]. The rotor blades have a rectangular planform with a NACA 0015 airfoil section. The rotor blades are nearly rigid, which allows for CFD analyses that neglect structural deformations. The advance ratio, $\mu = 0.10$, is selected for investigation, and the relevant blade angles and thrust coefficient are reported in Table 1. Data from this effort include instantaneous and time-averaged pressures along the fuselage, as well as vortex behavior via laser-light sheets. The

Table 1 Flow conditions and rotor parameters

Variable	Value
μ	0.10
V_{tip}, m/s	100.5
c, m	0.086
Re_c	577,870
β_{1s}, deg	−2.02
β_{1c}, deg	−1.94
C_T	0.009045

Table 2 Summary of tolerances applied for the different adaptation schemes

Method	Tolerance (F_{tol})
$|\omega|$	0.001
Δp	0.003
Nondimensional Q-criterion	0.01

fuselage station is nondimensionalized (x/R) by the rotor radius ($R = 0.4572$ m) for ease in presentation.

This model has been evaluated by numerous prior computational efforts with a variety of approaches (e.g., [1,2,40–43]). O'Brien [3] used this as a validation case for his series of actuator to overset rotor
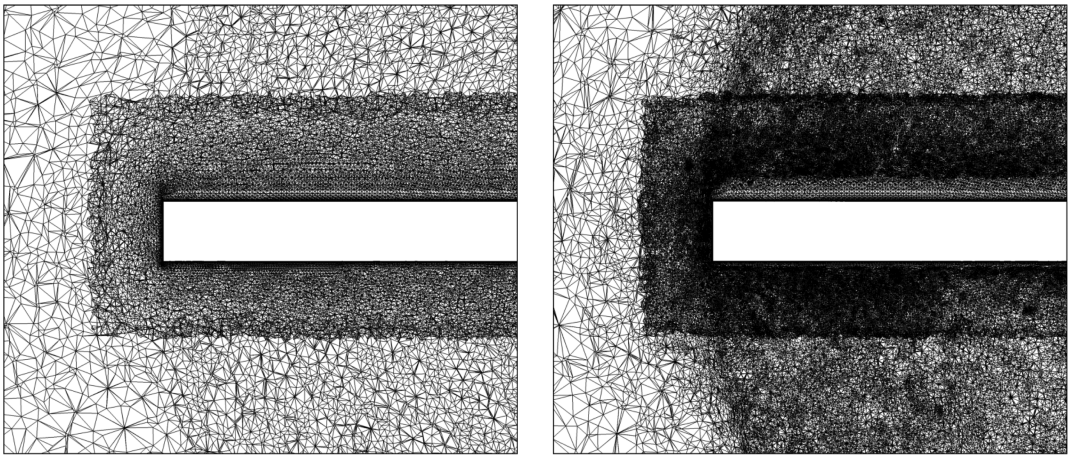

a) Initial grid   b) Adapted grid
Fig. 3   Grid comparison; view is of the blade plane from the top.
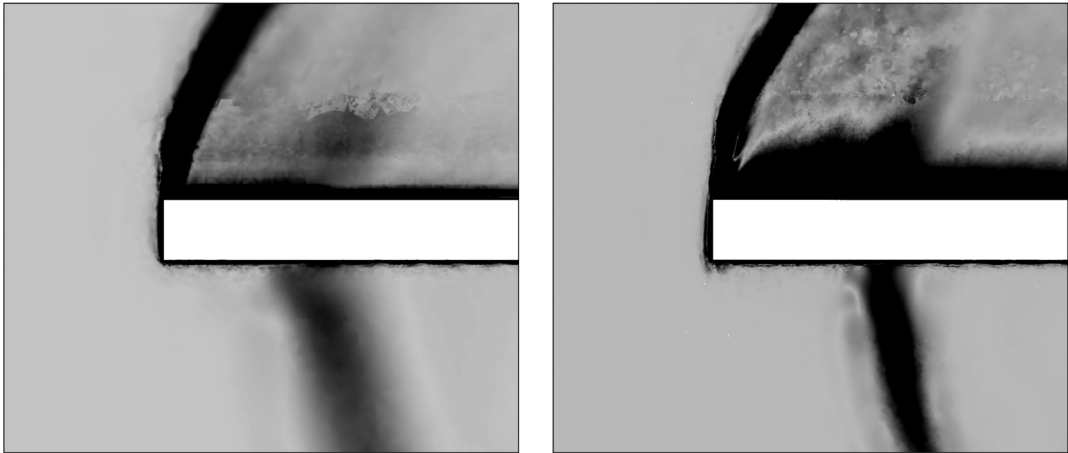

a) Initial grid   b) Adapted grid
Fig. 4   Vorticity-magnitude comparison; view is of the blade plane from the top.

Table 3   Inviscid simulations: summary of grid size resulting from the different adaptation schemes
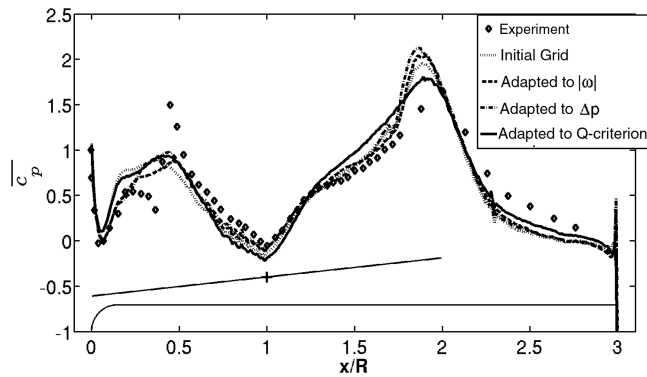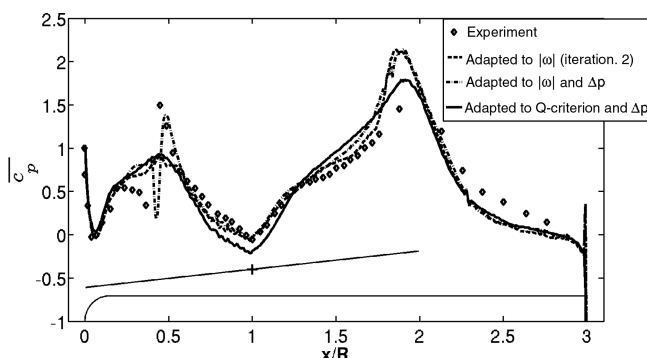
Scheme description	Total nodes (millions)
Initial grid	2.03
Adapted to $|\omega|$	6.68
Adapted to Δp	2.92
Adapted to Q-criterion	9.95
Adapted to $|\omega|$ (iteration 2)	12.8
Adapted to $|\omega|$ and Δp	8.86
Adapted to Q-criterion and Δp	23.3

models implemented into FUN3D. Numerous details of the time-averaged fuselage pressure coefficient have not been captured by these methods, in spite of the simplistic model geometry. O'Brien [3] noted that some time-averaged features just aft of the rotor were captured when the entire model (rotor strut and hub geometry) was included. The model investigated here does not include the hub-pin geometry. However, the vortex–fuselage impingement observed in the original experiments near the nose ($x/R \approx 0.3$) [39] has not been adequately resolved by any of these prior simulations. One major goal of this effort was to accurately capture this vortex–fuselage impingement.

The vortex/fuselage-impingement process is sketched in Fig. 2. Brand [39] describes the tip vortex from the prior blade dissociating into two circulatory regions due to the interaction with the following blade. These regions create primary and secondary vortex–fuselage interactions, in which the latter is characterized by circulation with a sense opposite to the primary tip vortex. As the flow progresses, Brand reports that the primary vortex interaction weakens and remains relatively stationary, whereas the secondary interaction is rapidly swept downstream.

B.   Approach

The adaptation methodology was initially tested using inviscid simulations, so that the best strategies could be applied for the more

expensive fully turbulent simulations. Solution advancement was performed with a time step equivalent to 1 deg azimuthal sweep. During each time step, a maximum of 40 subiterations were used in conjunction with the temporal error-control option [26] to ensure two orders of magnitude reduction in residual. The metric intersection was performed over a time window corresponding to 180 deg blade sweep or 180 steps after the solution became periodic (after two revolutions). The tolerance levels for the different feature-based schemes, primarily chosen based on solution interrogation, are given in Table 2. In order to obtain valid comparisons with the experiment, the computed thrust coefficient was ascertained to be within 1% of the experimental value listed in Table 1.

Subsequently, a turbulence-model study was performed to assess the efficacy of the $k\omega$-SST model against the *Georgia Institute of Technology* HRLES method with respect to prediction of the physics. Finally, fully turbulent computations were carried out to assess the validity of the most beneficial adaptation strategies.
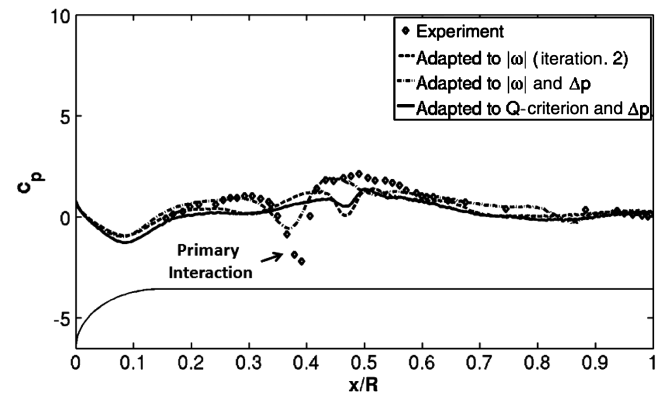
a) $\psi = 30°$
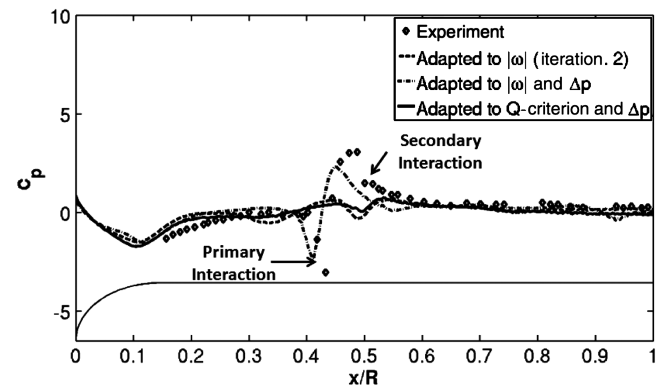
b) $\psi = 60°$
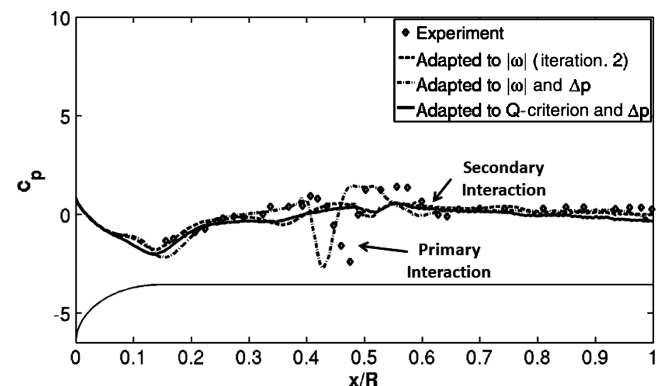
c) $\psi = 90°$

Fig. 7   Inviscid simulations: top centerline instantaneous pressures (first-quarter revolution).

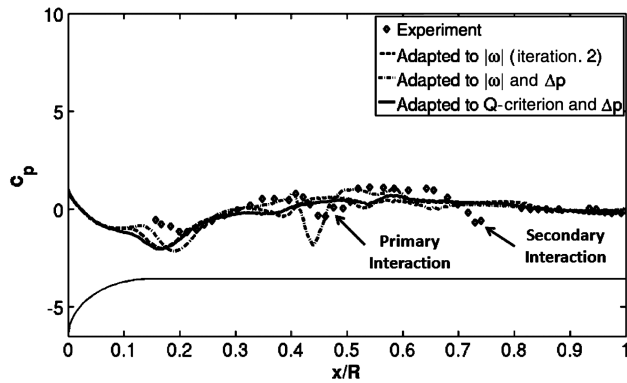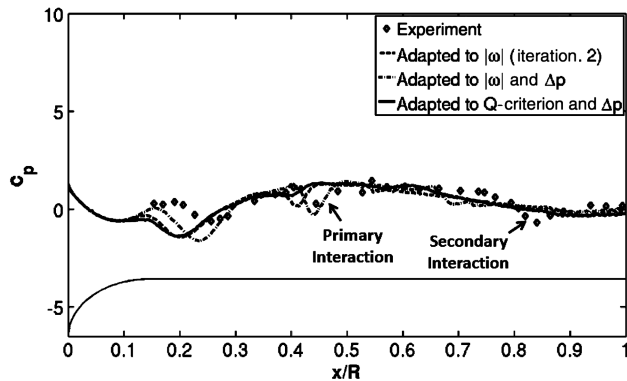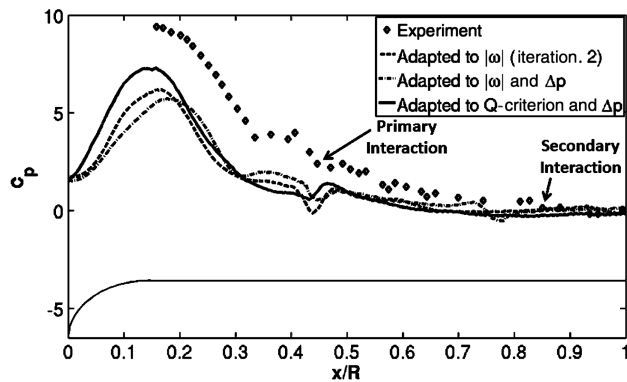**Fig. 5   Inviscid simulations: top centerline time-averaged pressures from one adaptive cycle.**

Fig. 6   Inviscid simulations: top centerline time-averaged pressures from two adaptive cycles.

a) $\psi = 120°$

b) $\psi = 150°$

c) $\psi = 180°$

Fig. 8   Inviscid simulations: top centerline instantaneous pressures (second-quarter revolution).

### C.   Methodology Demonstration

The ability of this new methodology to capture complex unsteady features in the flowfield is confirmed in Figs. 3 and 4. Figure 3a illustrates the initial grid, and the distinction between the background and blade grids can be easily observed. The tip vortex diffuses as it passes from the blade grid to the fuselage grid, observed in Fig. 4a. Using a new grid adapted to $|\omega|$ and Δp (over two cycles) captures the previous tip vortex as it interacts with the blade, as shown in Figs. 3 and 4b. Furthermore, the overset-adaptation capability clearly allows these features to pass seamlessly between the blade grid and the fuselage grid.

IV.   Results

A.   Inviscid Simulations

Several feature-based adaptations were evaluated for the Georgia Institute of Technology RFI configuration to determine the validity of the method, as well as the appropriate flowfield adaptation feature. Table 3 details the grid sizes resulting from the initial grid to the different feature-based schemes that were studied. The initial grid contained prerefinement in the expected rotor-wake region. The first three adaptation schemes ($|\omega|$, Δp, and Q-criterion) apply grid modifications on the initial grid. The following three schemes are double adaptation schemes, that is, they use the solution from one of the previous adaptation schemes and adapt that grid a second time using the same or a different feature. The grid initially adapted to $|\omega|$ is again adapted to $|\omega|$, referred to as the $|\omega|$ (iteration 2) scheme. In an alternate fashion, the grid originally adapted to $|\omega|$ is adapted to Δp, referred to as the vorticity-mixed scheme. The final scheme uses the grid initially adapted to the Q-criterion and adapts it to Δp, henceforth referred to as the Q-criterion-mixed scheme. Double adaptation to Δp is not included because of its inability to sufficiently capture the tip-vortex intensity. Also, because double adaptation to $|\omega|$ was found to be ineffective, and because both the $|\omega|$ and the Q-criterion target high-vorticity regions such as tip vortices, double adaptation to the Q-criterion was also not considered.

The Δp adaptation, resulted in a much more efficient adaptation than the $|\omega|$ and Q-criterion-based schemes, based solely on the grid size (Table 3). Only minor differences between the $|\omega|$ and Δp schemes were observed for the time-averaged fuselage pressure coefficient $\bar{c}_p$ peaks at the $x/R = 0.5$ and 2.0 locations (Fig. 5) after one cycle. With the exception of the Q-criterion scheme, the result of the first adaptation was to refine the initial vortex interaction at the nose ($x/R = 0.1$), so that the magnitude and pressure rise are more adequately captured. The Q-criterion scheme does not differ greatly from the initial grid at $0.2 \leq x/R \leq 0.5$, but shows significant differences from all the other schemes at and behind the hub region $x/R \geq 1$. The effects of the vortex shed from the second blade, observed in the pressures along $0.2 \leq x/R \leq 0.5$, are not captured with either the baseline or the single adaptation. The vortex–fuselage
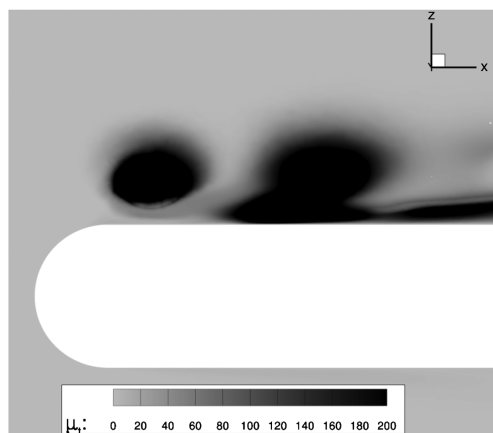
a) Eddy viscosity
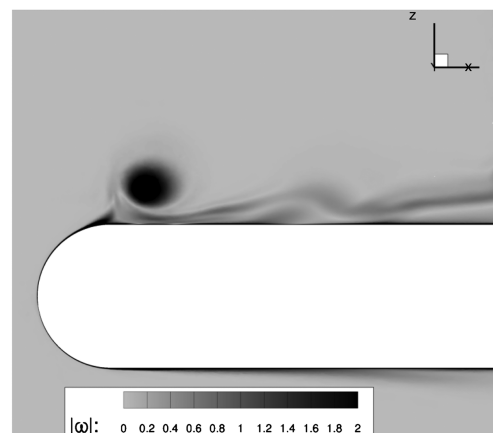
b) Vorticity magnitude

Fig. 9   Contours along the airframe symmetry plane from the $k\omega$-SST model.

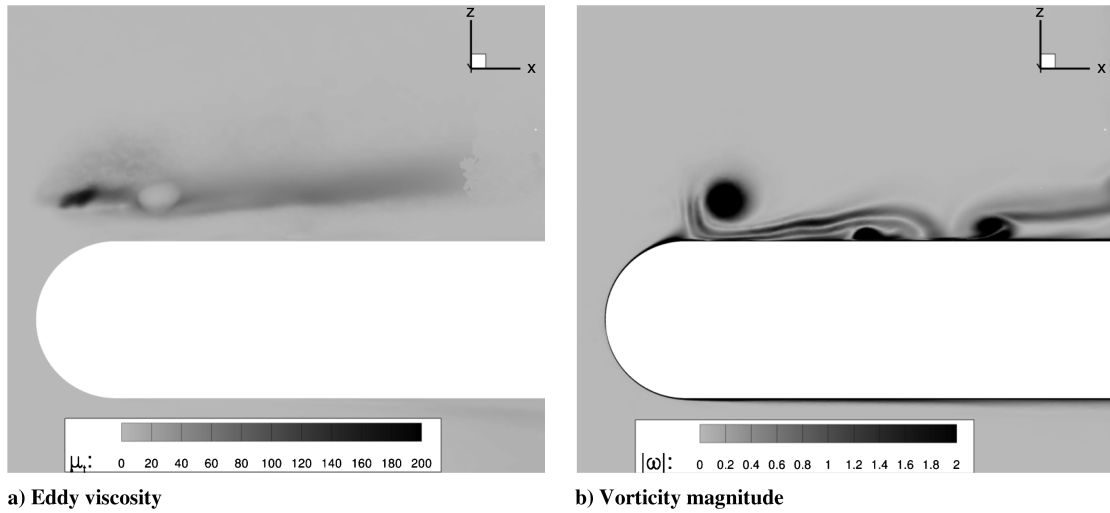a) Eddy viscosity   b) Vorticity magnitude

Fig. 10   Contours along the airframe symmetry plane from the HRLES model.

interaction at $x/R = 2.3$ is captured by all three meshes as a weak pressure pulse, and the magnitude does not change with grid adaptation, although a minor ($x/R < 0.05$) shift forward is observed upon grid adaptation.

The results of the second adaptation are much more significant (Fig. 6). While the $|\omega|$ (iteration 2) scheme results in a much larger mesh size, its influence on the fuselage pressure characteristics is minimal. On the other hand, the vorticity-mixed scheme yields significant improvement, and employs about 75% of the mesh required by double adaptation to $|\omega|$. This scheme captures the vortex–fuselage interaction described by Brand [39], denoted by the sharp rise in pressure for $0.4 \le x/R \le 0.5$. Adapting the grid using the Q-criterion-mixed scheme obtains improvement in the average pressures in the nose region, but it does not improve the pressures where the vortex–fuselage interaction exists.

Further examining the instantaneous flowfield (Figs. 7 and 8), the characterizations noted in the time-averaged pressures are reenforced in these data. For the first-quarter revolution, in which the rotor blades depart from the fuselage (Fig. 7), the $|\omega|$ (iteration 2) scheme and the Q-criterion-mixed scheme improve the instantaneous pressure prediction only slightly, and include a significant lag ($\Delta x/R \approx 0.1$) in the location of the primary vortex interaction at $0.4 \le x/R \le 0.5$. The vorticity-mixed scheme still shows lower magnitude at $\psi = 30$ and 60 deg due to an apparent phase lag of this vortex interaction, particularly at $\psi = 90$ deg; however, the results are significantly improved over the single adaptation. It is also important to note that the magnitude and character of the pressure rise resulting from the primary interaction, which is completely missed by the baseline and other adaptation schemes, are overall well captured. Minor differences are observed in the centerline pressure exclusive of this vortex interaction.

As observed in Fig. 8, the second quarter of the rotor revolution continues this overall trend, but with increasing differences with the experiment as the two rotor blades approach the fuselage back to their original positions. Again, the primary vortex interaction at $0.4 \le x/R \le 0.5$ continues to be more accurately captured with the
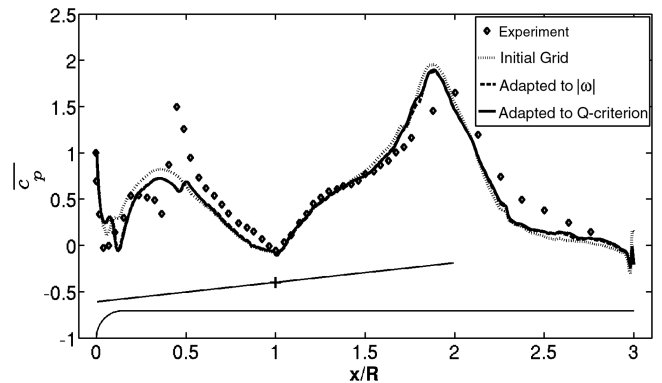

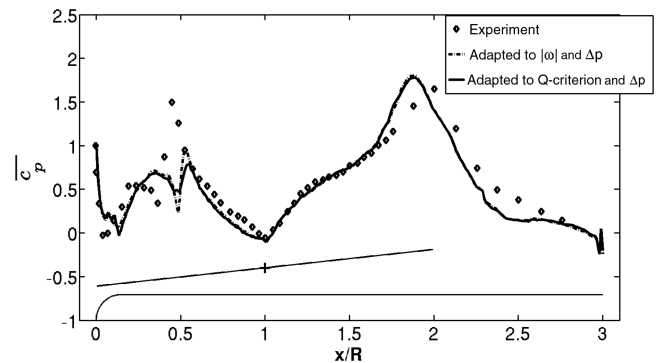Fig. 11   HRLES: time-averaged pressures on the top centerline from one adaptive cycle.

Fig. 12   HRLES: time-averaged pressures on the top centerline from two adaptive cycles.

vorticity-mixed scheme. The secondary vortex interaction in the range $0.7 \le x/R \le 0.9$ during this quarter is not captured by either the $|\omega|$ (iteration 2) scheme or the Q-criterion-mixed scheme. The vorticity-mixed scheme appears to capture this feature, albeit early, and as a weaker interaction at $\psi = 120$ and 150 deg. The significant high pressure region near the nose and forward portion of the fuselage ($0.2 \le x/R \le 0.5$) at $\psi = 180$ deg when the blades are directly over the fuselage is not predicted using any method. Overall, however, it is evident that the vorticity-mixed scheme clearly most accurately predicts instantaneous pressures among the various schemes evaluated. The inability of the Q-criterion-mixed scheme to mimic the vorticity-mixed scheme in these inviscid simulations is discussed later.

Table 4   HRLES: summary of grid size resulting from the different adaptation schemes

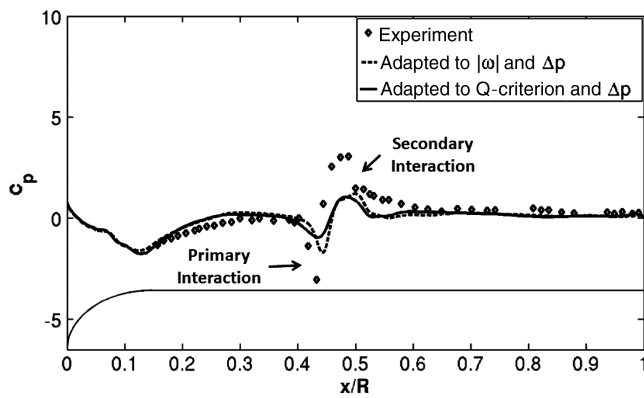| Scheme description	Total nodes (millions)
Initial grid	5.52
Adapted to $|\omega|$	13.0
Adapted to Q-criterion	16.8
Adapted to $|\omega|$ and Δp	24.2
Adapted to Q-criterion and Δp	30.7

B. Turbulence-Model Study

The capability of this adaptation methodology to capture viscous flow phenomena was considered. Two turbulence methods, a RANS model ($k\omega$-SST) and an HRLES model, were studied. The HRLES model combines the $k\omega$-SST model with large-eddy simulation (LES) by calculating the turbulence kinetic energy (TKE) at every grid node in the domain. The RANS calculation of TKE is complemented with an LES calculation using a k_{sgs} equation. A blending function is then used to weight the calculation between the RANS- and the LES-dominated regions of flow [29]. The blending function permits a RANS–LES weighted calculation of TKE and eddy viscosity μ_t [44].
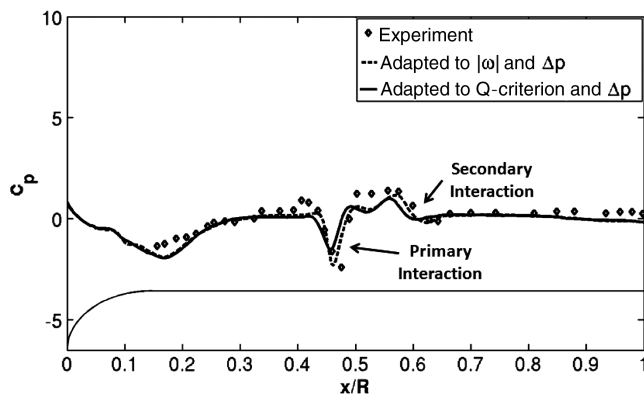
Using a highly prerefined composite grid (15.4 million nodes), wherein the background grid was refined in the wake region between the blade and the fuselage, the effect of tip-vortex dissipation is studied by applying both these turbulence models. The eddy viscosity and vorticity magnitude predicted using the $k\omega$-SST model and the HRLES model are shown in Figs. 9 and 10, respectively.

These figures depict the prediction at $\psi = 120$ deg, but the same result is obtained at different blade azimuths.

Two observations can be made with respect to Figs. 9 and 10. First, the eddy-viscosity prediction from the $k\omega$-SST simulation is significantly higher and widespread in the region coinciding with the forward tip vortex. The vortex also appears to be visibly diffused or spread out in comparison to the HRLES prediction. Furthermore, the vortex-core region of the HRLES simulation predicts significantly lower eddy viscosity, implying that this vortex core exhibits expected laminar behavior. The other observation is that the high eddy-viscosity prediction from the $k\omega$-SST simulation that dominates the rotor-wake region clearly diffuses the vortex propagating toward the fuselage following interaction with the oncoming blade. Additionally, the rotor-wake vorticity contours of the HRLES computation show two distinct high-vorticity regions that are characteristic of the expected vortex–fuselage interaction. This study demonstrates the superiority of the HRLES model in the preservation of the tip vortex and in capturing a more complex interaction with the subsequent blade passage.
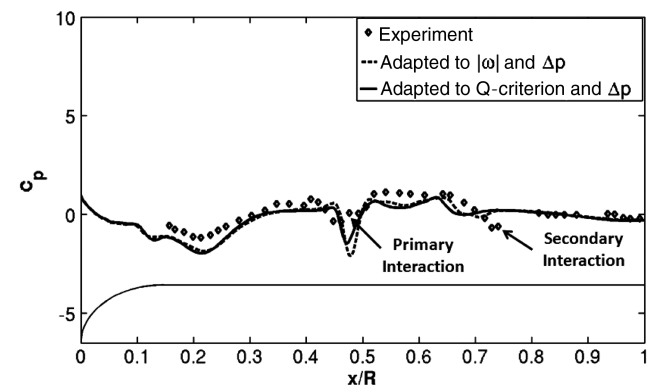

a) $\psi = 30^\circ$

b) $\psi = 60^\circ$

c) $\psi = 90^\circ$
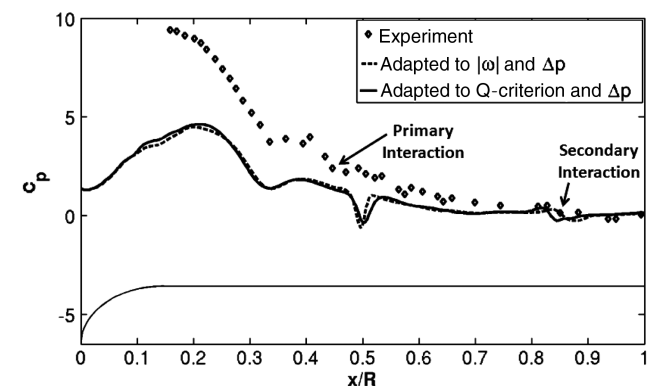
Fig. 13   HRLES: top centerline instantaneous pressures (first-quarter revolution).

a) $\psi = 120^\circ$
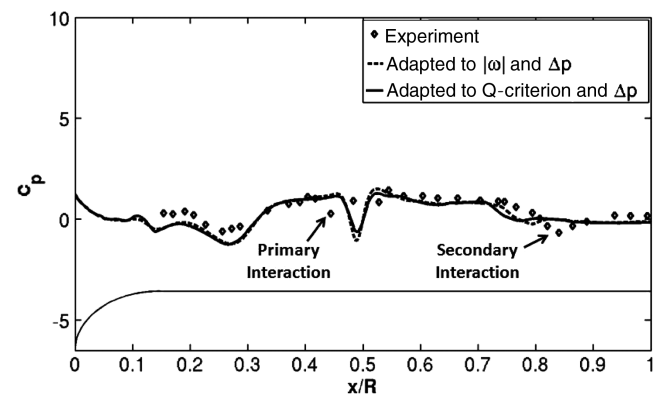
b) $\psi = 150^\circ$

c) $\psi = 180^\circ$

Fig. 14   HRLES: top centerline instantaneous pressures (second-quarter revolution).

C. HRLES Computations

The initial grid used for the HRLES computations had the same prerefinement in the rotor-wake region as in the inviscid simulations. The major difference is the addition of a boundary-layer grid with a $y^+ = 1$ and at least 35 boundary-layer cells. Mixed elements are used to generate this boundary-layer grid, allowing for accurate simulations with the HRLES turbulence model [29]. The grid sizes resulting from the initial grid to the different feature-based schemes are listed in Table 4. Among the single adaptation schemes, adaptation to Δp was not considered because of its inability to preserve regions of high vorticity, which are essential to capture the magnitude of the fuselage surface pressures. The double adaptation schemes studied were the vorticity-mixed scheme and the Q-criterion-mixed scheme. The $|\omega|$ (iteration 2) scheme was not performed because the inviscid simulations showed very little improvement from the single adaptation to $|\omega|$.

Time-averaged fuselage pressures comparing the $|\omega|$ and the Q-criterion single adaptation schemes (Fig. 11) show very small differences, unlike the results from the inviscid simulation (Fig. 5). Both these schemes improve the magnitude of the pressures in the forward part of the fuselage ($x/R \leq 0.3$), with exception to the nose region. Additionally, the primary vortex interaction resulting from both these schemes indicates the presence of a small pressure pulse at $x/R \approx 0.5$.

The vorticity-mixed scheme and the Q-criterion-mixed scheme improve the accuracy of the time-averaged pressures (Fig. 12), particularly in predicting the intensity of the primary vortex interaction $x/R \approx 0.5$. Both schemes have clear similarities, but the vorticity-mixed scheme predicts a stronger pressure pulse than the Q-criterion-mixed scheme. Again, because the hub-pin geometry is not modeled [3], the HRLES computations are not able to accurately predict the pressures in the aft portion of the rotor ($x/R > 1.5$).

The instantaneous fuselage pressures, plotted in Figs. 13 and 14, show good correlation with experimental data at intermediate azimuths ($\psi = 90$-150 deg) with both the vorticity-mixed scheme and the Q-criterion-mixed scheme. Both schemes agree very well with each other, and the only difference observed is that the vorticity-mixed scheme predicts a higher magnitude of the primary vortex interaction. With respect to the experiment, both schemes result in a small lead ($\Delta x/R = 0.01$) in the spatial location for the primary vortex interaction. The magnitude of the interaction is underpredicted for the first-quarter revolution, and is overpredicted for the second-quarter revolution. The secondary vortex interaction initially shows a slight lead in the spatial location ($\Delta x/R = 0.05$), but during the second-quarter revolution, this interaction lags behind the experiment by the same amount. The faster convection rate of the secondary vortex interaction is not captured. This may be attributable to the boundary-layer effects not being modeled as accurately either due to
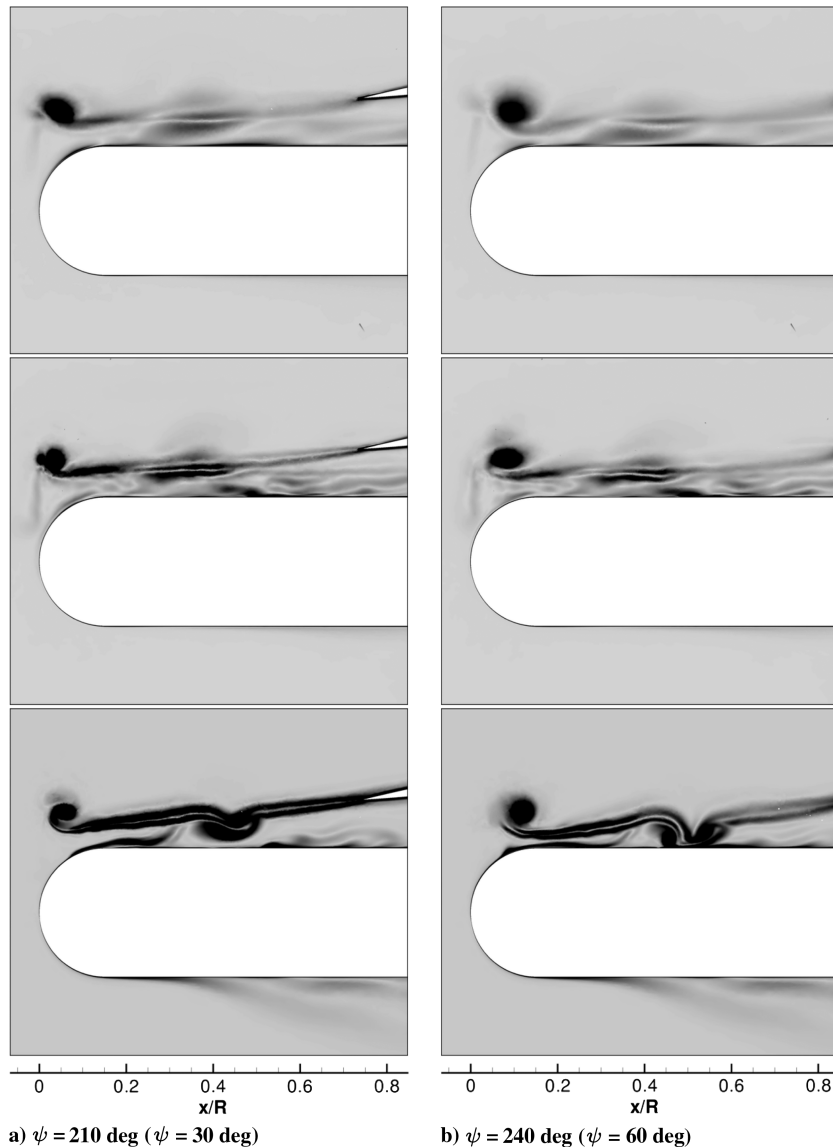

a) $\psi = 210$ deg ($\psi = 30$ deg)   b) $\psi = 240$ deg ($\psi = 60$ deg)

Fig. 15   Vortex behavior (from top: initial grid, adapted to $|\omega|$, and vorticity-mixed scheme).

lack of adaptation or shortcomings of the turbulence modeling in this region. As with the inviscid simulations, the high-pressure regions in the forward portion of the fuselage ($0.2 \leq x/R \leq 0.5$) at $\psi = 180$ deg do not correlate well.

To further understand the significance of the grid refinement in each scheme, the vortex behavior is examined in Figs. 15–17. The adaptation sequence from the initial grid to the vorticity-mixed scheme is plotted from top to bottom at each selected azimuthal location. Because the adaptation sequence leading to the Q-criterion-mixed scheme shows similar results as with the vorticity-mixed scheme, it is not presented here. It is clear from scanning from top to bottom that the forward vortex core is more crisply predicted after the first adaptation (middle plot), and refined further upon the second adaptation (bottom plot). In addition, the initially weaker vortical features in the rotor wake, diffused over large areas, become further defined due to adaptation.

Differences between the various adaptation schemes can also be discerned from the magnitude and shape of the vorticity contours in these figures. For example, the shape of the vortex at $0.4 \leq x/R \leq 0.5$, where the primary interaction occurs, is very different. Specifically, tracing the vorticity-mixed scheme across Figs. 15–17, it is possible to discern the path of the tip vortex as it leaves the blade, interacts with the previous blade's wake sheet, and finally collides with and encompasses the fuselage centerline. Brand [39] reported

that the tip vortex from the prior blade interacts with the following blade at $x/R = 0.3$ at $\psi = 188$ deg (or $\psi = 8$ deg), which is comparable to the grid-adaptation results in Fig. 17b. The weakening vorticity of the primary interaction, observed at approximately $x/R = 0.45$ in Figs. 15–17, correlates to the experimental visualization, as sketched in Fig. 2. The vortex-sheet roll-up, which was experimentally observed to traverse in the range $0.4 \leq x/R \leq 0.5$ during this azimuthal time period, has also been observed traveling downstream at $\psi = 210$ deg, and with a distinct rotation by $\psi = 240$ deg, located in the same fuselage locations. The development of the secondary vortex–fuselage interaction and its subsequent rapid downstream convection (Fig. 2b) is also observed in the vorticity-mixed scheme and the Q-criterion-mixed scheme (not shown).

D. Vorticity–Q-Criterion Discrepancy

The reason why there is a lack of agreement between the vorticity-mixed and Q-criterion-mixed schemes in the inviscid simulations but not in the viscous simulations has been investigated. The Q-criterion-indicator formulation targets regions where the rotation rate $\|\Omega\|$ dominates the strain rate $\|S\|$, because $F_{\text{tol}} = 0.01$. In regions where $\|S\|$ exceeds $\|\Omega\|$, the Q-criterion (dimensional or nondimensional) values are negative. Therefore, such regions are not selected for refinement. The vorticity-magnitude method, on the other hand, does not discriminate regions where strain rates dominate, and its range is
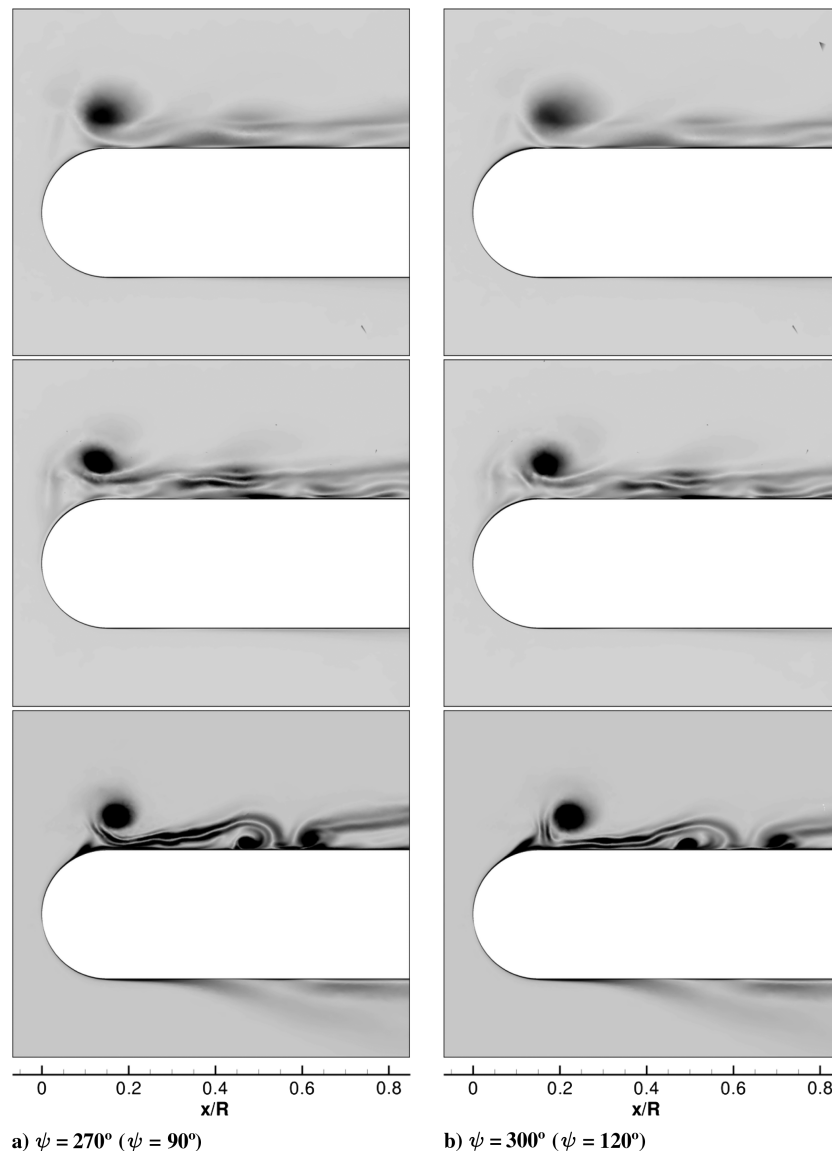

a) $\psi = 270°$ ($\psi = 90°$) b) $\psi = 300°$ ($\psi = 120°$)

Fig. 16 Vortex behavior (from top: initial grid, adapted to $|\omega|$, and vorticity-mixed scheme).

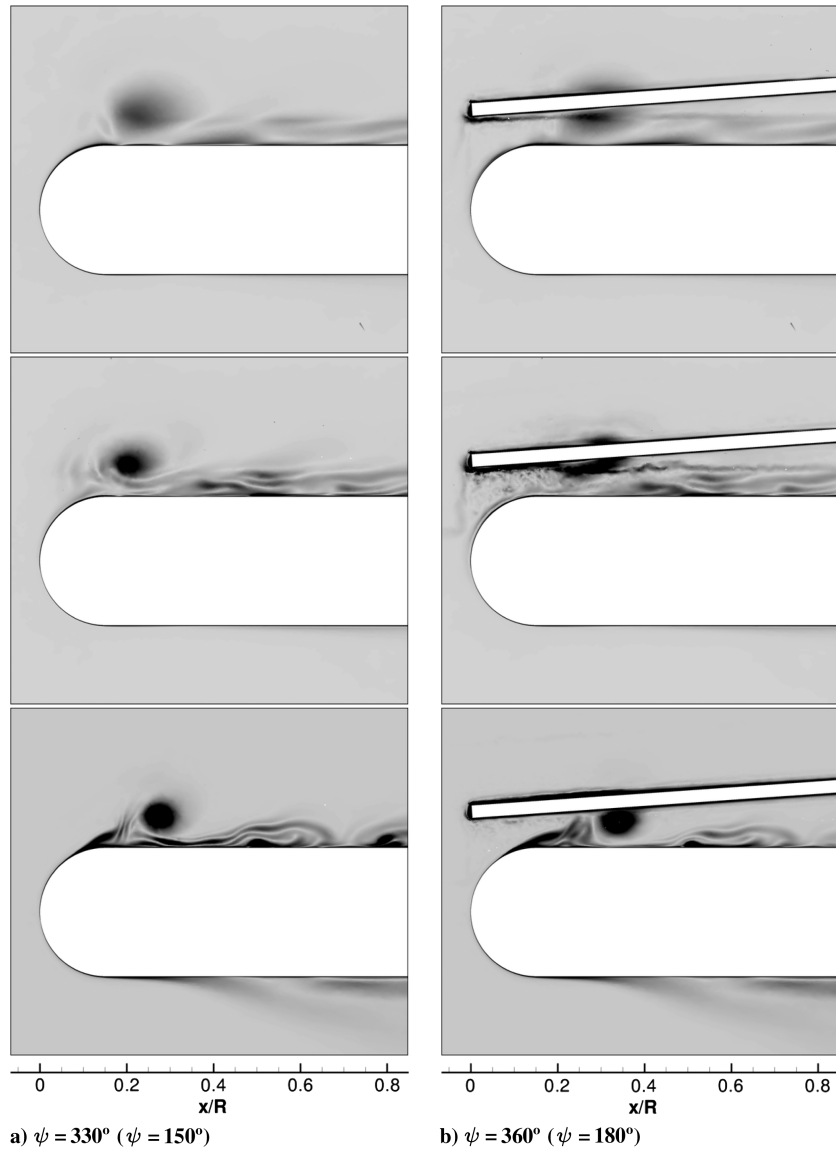a) $\psi = 330^{\circ}$ ($\psi = 150^{\circ}$)   b) $\psi = 360^{\circ}$ ($\psi = 180^{\circ}$)

Fig. 17   Vortex behavior (from top: initial grid, adapted to $|\omega|$, and vorticity-mixed scheme).

always nonnegative. Figure 18 illustrates the differences in the flowfields resulting from these schemes for the inviscid simulations. The vortex-sheet region clearly displays uniformly high values of vorticity, but the values of the Q-criterion in those regions are

negative or very close to zero. Regions where both the vorticity-magnitude and the Q-criterion are high include the vortex-core region and few localized regions in the vortex sheet. The fully turbulent flowfields resulting from these adaptation schemes are compared in
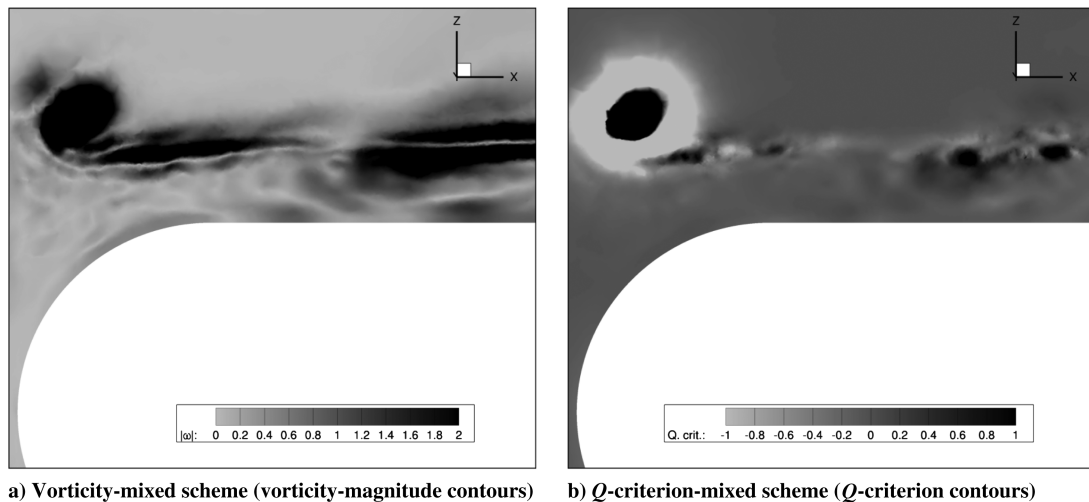

a) Vorticity-mixed scheme (vorticity-magnitude contours)   b) Q-criterion-mixed scheme (Q-criterion contours)

Fig. 18   Inviscid simulations: comparison of the vorticity-mixed and Q-criterion-mixed schemes.

Fig. 19. High values of vorticity throughout the vortex sheet are observed in Fig. 19a. In comparison to Fig. 18b, the vortex sheet in Fig. 19b shows several more spots of positive Q-criterion values. Therefore, these regions in the vortex sheet are selected for refinement in the turbulent simulation, and are excluded from refinement in the inviscid simulation. Because the adaptation metric is accumulated over 180 deg azimuthal sweep, the highly refined vortex sheet benefits the preservation of the tip vortex as it passes through these regions. Another difference between inviscid and turbulent simulations is that the latter exhibits an interaction with the rotor wake and fuselage boundary layer about the juncture of the hemispherical nose and cylindrical fuselage. This region indicates both high values of vorticity magnitude and positive Q-criterion. This behavior arises mainly due to the no-slip boundary condition of the turbulent simulations.

The genesis of the positive Q-criterion values in the turbulent vortex sheet is explained by examining the flowfield near the blade trailing edge in Fig. 20. The trailing-edge region exhibits high-Q-criterion values over a significant portion of the blade span for the turbulent simulation, absent from the inviscid simulation. This is attributed to boundary-layer/trailing-edge vortex shedding due to the blade's no-slip boundary condition.

E. Tip-Vortex Behavior

Experimental visualizations document the tip-vortex locations as soon as they become visible at $\psi = 188$ deg, and are plotted at 30 deg intervals until impingement with the fuselage in Fig. 21a. Vortex locations from the vorticity-mixed scheme, resulting from both the inviscid and HRLES computations, are shown in comparison to the experiment. Figure 21b plots the streamwise spatial location lead (or lag) with respect to the experiment. Both simulations show the same lead at the first vortex location. However, the inviscid simulation shows a vortex lag for the rest of the azimuthal locations, as high as $\Delta x/R = 0.032$. These results are corroborated by the instantaneous fuselage pressures in Figs. 7 and 8. The HRLES prediction correlates much better, generally leading the experiment, with the maximum vortex lead of $\Delta x/R = 0.013$. This spatial lead is also observed via the surface pressures in Figs. 13 and 14. The uncertainty in the streamwise location reported with the experiment was 15 mm or $\Delta x/R = 0.033$. Both simulations with the vorticity-mixed scheme are within the experimental error, but Fig. 21b shows significantly better spatial correlation from the HRLES computation of the vortex location.

F. Adaptation Convergence

The convergence of this feature-based adaptation process has been assessed by evaluating an integrated quantity of interest obtained over a series of adaptation cycles. Because the time-averaged pressure distribution has been previously applied as a suitability criterion of an adaptation scheme, the time-averaged centerline pressure integral is used here to identify convergence. The functional quantity is
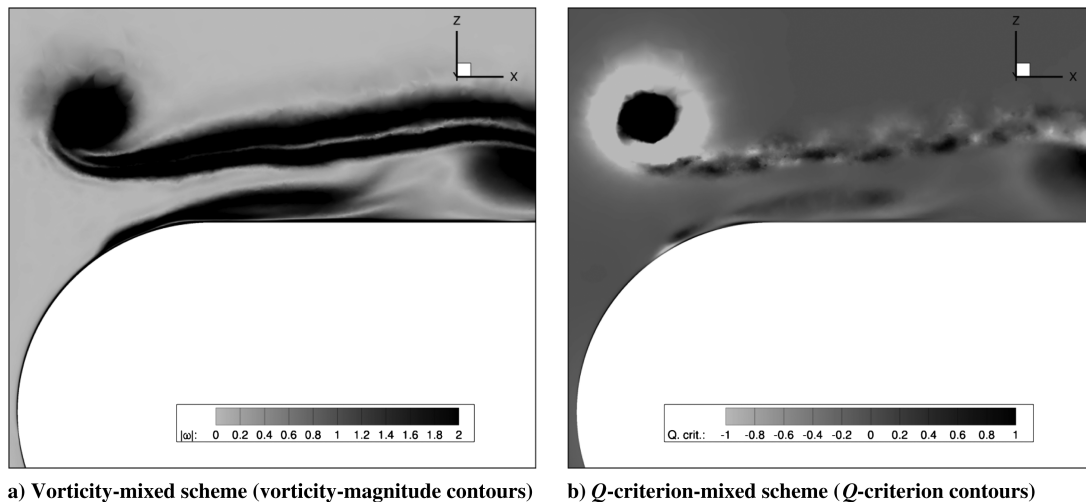

a) Vorticity-mixed scheme (vorticity-magnitude contours) b) Q-criterion-mixed scheme (Q-criterion contours)
Fig. 19 HRLES: comparison of the vorticity-mixed and Q-criterion-mixed schemes.
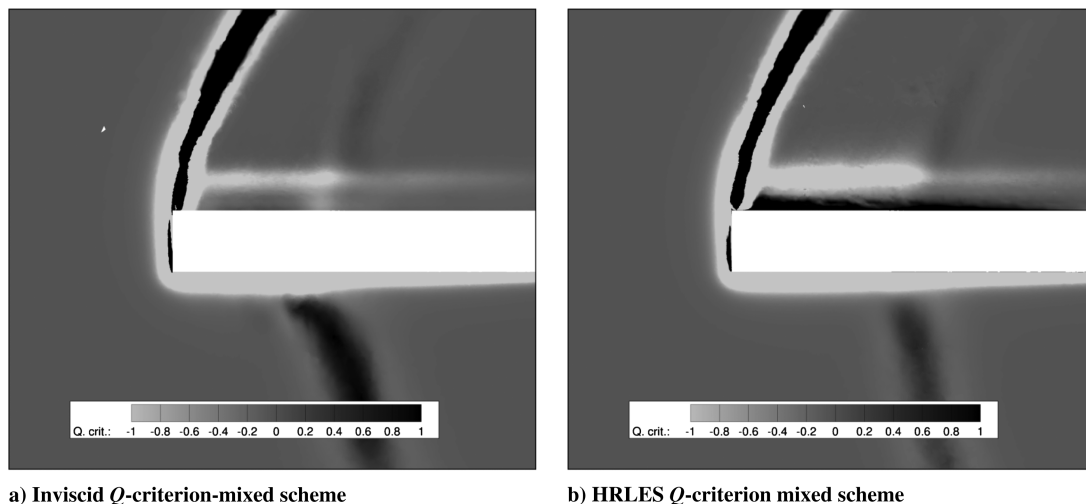

a) Inviscid Q-criterion-mixed scheme b) HRLES Q-criterion mixed scheme
Fig. 20 Comparison of inviscid and viscous modeling of the flowfield for the Q-criterion-mixed scheme.

a) Vortex paths

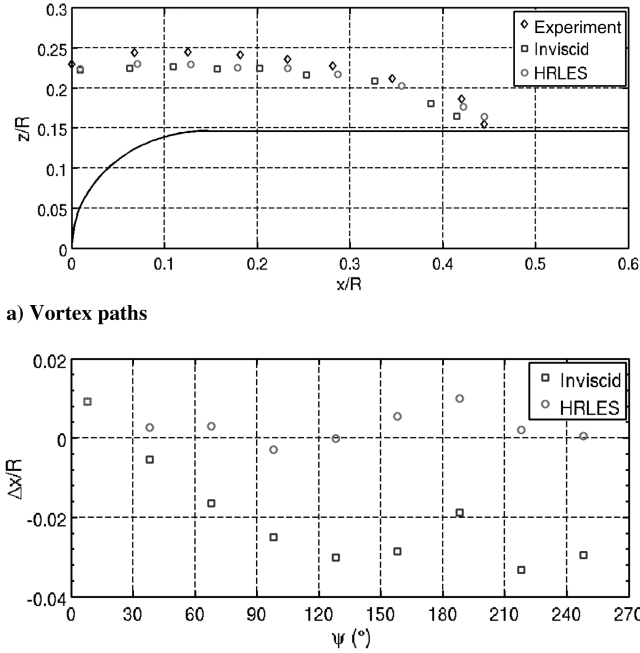**b) Streamwise location lead (positive) vs azimuth**

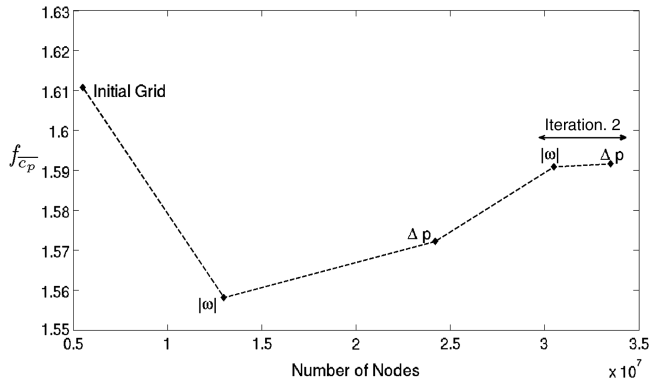**Fig. 21 Vortex-trajectory comparisons from the vorticity-mixed scheme.**

Fig. 22 Pressure-integral functional convergence for the HRLES vorticity-mixed scheme.

$$f_{\bar{c}_p} = \int_0^{3R} \bar{c}_p \, \mathrm{d}x \qquad (8)$$

in which the fuselage length is $3R$.

The convergence of the vorticity-mixed scheme has been assessed by performing an additional adaptation sequence (i.e., additional adaptations that include both the $|\omega|$ and the Δp). The pressure integral is plotted in Fig. 22 for the vorticity-mixed HRLES computation. Convergence is established for the four adaptation cycles because the change in the functional between cycles 3 and 4 is observed to be within 0.05%.

The efficacy of the overset time-accurate grid-adaptation capability has been demonstrated, but the solution dependency on the selection of the feature or combinations of features is clear. In addition, any uncertainty in the number of adaptation cycles suggests that a method to directly relate convergence to the functional of interest is required, such as adjoint-based adaptation. Adjoint-based adaptation has been demonstrated for steady single grids by Park [32] and Park and Carlson [45]. The extension of adjoint-based-adaptation capability to include overset time-accurate simulations may be warranted.

V. Conclusions

A new grid-adaptation methodology has been developed and demonstrated to permit time-dependent adaptation across overset unstructured meshes. The methodology has been successfully demonstrated on an RFI configuration. In particular, the following observations can be made:

1) A single grid-adaptation framework has been extended to overset grid systems to allow for large relative motion. This required a strategy to identify, track, and reconstruct the component grid that each node is located within.

2) Demonstration on an RFI case illustrates the solution dependency on the feature selection and the number of adaptation cycles.

3) Flowfield features and fuselage pressures require a minimum of two grid-adaptation cycles. The most accurate adaptation scheme for the inviscid simulations is the vorticity-mixed scheme. Both the vorticity-mixed scheme and the Q-criterion-mixed scheme show accurate results for the HRLES computations.

4) The HRLES turbulence model is significantly superior than the $k\omega$-SST RANS model in the preservation of rotor-wake features. The high-eddy-viscosity prediction resulting from the $k\omega$-SST model significantly dissipates the features contributing to the vortex–fuselage interaction.

5) The ability of the current formulation of the Q-criterion-mixed scheme to capture some features in viscous near-body flows is limited by its inability to adapt in regions where strain rates dominate rotation rates, such as the vortex sheet.

6) The effect of modeling the flow as either inviscid or fully turbulent affects the rate of convection of the tip vortex until fuselage impingement. The vorticity-mixed scheme from the inviscid simulation shows a general spatial lag of the tip-vortex location, whereas the same for the HRLES computation shows a slight lead.

7) The uncertainty associated with the selection of the adaptation feature and the number of adaptation cycles imply that a more rigorous adaptation process, such as adjoint-based adaptation, may be more appropriate than feature-based adaptation. Future efforts will focus on the development of an adaptation process that will circumvent the issues identified with feature-based adaptation, as well as extension of the method to other rotorcraft-related applications.

Acknowledgments

References

[1] Ruffin, S. M., O'Brien, D. M., Smith, M. J., Hariharan, N. S., Lee, J. D., and Sankar, L., "Comparison of Rotor–Airframe Interaction Utilizing Overset and Unstructured Grid Techniques," AIAA Paper 2004-0046, Jan. 2004.

[2] O'Brien, D. M. Jr., and Smith, M. J., "Understanding the Physical Implications of Approximate Rotor Methods Using an Unstructured CFD Method," *Proceedings of the 31st European Rotorcraft Forum*, Curran Associates, Inc., Red Hook, NY, 2005, pp. 798–816.

[3] O'Brien, D. M., "Analysis of Computational Modeling Techniques for Complete Rotorcraft Configurations," Ph.D. Thesis, Georgia Inst. of Technology, Atlanta, 2006.

[4] Potsdam, M., Smith, M., and Renaud, T., "Unsteady Computations of Rotor–Fuselage Interaction," *Proceedings of the 35th European*

Rotorcraft Forum, Curran Associates, Inc., Red Hook, NY, 2009, pp. 513–535.

[5] Smith, M. J., Shenoy, R., Kenyon, A. R., and Brown, R. E., "Vorticity-Transport and Unstructured RANS Investigation of Rotor–Fuselage Interactions," *Proceedings of the 35th European Rotorcraft Forum*, Curran Associates, Inc., Red Hook, NY, 2009, pp. 494–512.

[6] Komerath, N., Smith, M., and Tung, C., "A Review of Rotor Wake Physics and Modeling," *Journal of the American Helicopter Society*, Vol. 56, No. 2, 2011, pp. 1–19.
doi:10.4050/JAHS.56.022006

[7] Kang, H., and Kwon, O., "Effect of Wake Adaptation on Rotor Hover Simulations Using Unstructured Meshes," *Journal of Aircraft*, Vol. 38, No. 5, 2001, pp. 868–877.
doi:10.2514/2.2846

[8] Kang, H., and Kwon, O., "Unstructured Mesh Navier–Stokes Calculations of the Flow Field of a Helicopter Rotor in Hover," *Journal of the American Helicopter Society*, Vol. 47, No. 2, 2002, pp. 90–99.
doi:10.4050/JAHS.47.90

[9] Dindar, M., Shepherd, M., Flaherty, J., and Jansen, K., "Adaptive CFD Analysis for Rotorcraft Aerodynamics," *Computer Methods in Applied Mechanics and Engineering*, Vol. 189, No. 4, 2000, pp. 1055–1076.
doi:10.1016/S0045-7825(99)00368-0

[10] Potsdam, M., and Mavriplis, D., "Unstructured Mesh CFD Aerodynamic Analysis of the NREL Phase VI Rotor," AIAA Paper 2009-1221, Jan. 2009.

[11] Nam, H., Park, Y., and Kwon, O., "Simulation of Unsteady Rotor–Fuselage Interactions Using Unstructured Adaptive Sliding Meshes," *Journal of the American Helicopter Society*, Vol. 51, No. 2, 2006, pp. 141–149.
doi:10.4050/JAHS.51.141

[12] Cavallo, P., Sinha, N., and Feldman, G., "Parallel Unstructured Mesh Adaptation Method for Moving Body Applications," *AIAA Journal*, Vol. 43, No. 9, 2006, pp. 1937–1945.
doi:10.2514/1.7818

[13] Meakin, R., "On Adaptive Refinement and Overset Structured Grids," AIAA Paper 1997-1858, June–July 1997.

[14] Henshaw, W., and Schwendeman, D., "Parallel Computation of Three-Dimensional Flows Using Overlapping Grids with Adaptive Mesh Refinement," *Journal of Computational Physics*, Vol. 227, No. 16, 2008, pp. 7469–7502.
doi:10.1016/j.jcp.2008.04.033

[15] Kannan, R., and Wang, Z., "Overset Adaptive Cartesian/Prism Grid Method for Stationary and Moving-Boundary Flow Problems," *AIAA Journal*, Vol. 45, No. 7, 2007, pp. 1774–1779.
doi:10.2514/1.24200

[16] Canonne, E., Benoit, C., and Jeanfaivre, G., "Cylindrical Mesh Adaptation for Isolated Rotors in Hover," *Aerospace Science and Technology*, Vol. 8, No. 1, 2004, pp. 1–10.
doi:10.1016/j.ast.2003.08.008

[17] Duque, E., Biswas, R., and Strawn, R., "A Solution Adaptive Structured/Unstructured Overset Grid Flow Solver with Applications to Helicopter Rotor Flows," AIAA Paper 1995-1766, June 1995.

[18] Sankaran, V., Sitaraman, J., Wissink, A., Datta, D., Jayaraman, B., Potsdam, M., Mavriplis, D., Yang, Z., O'Brien, D., Saberi, H., Cheng, R., Hariharan, N., and Strawn, R., "Application of Helios Computational Platform to Rotorcraft Flowfields," AIAA Paper 2010-1230, Jan. 2010.

[19] Wissink, A. M., Kamkar, S., Pulliam, T. H., Sitaraman, J., and Sankaran, V., "Cartesian Adaptive Mesh Refinement for Rotorcraft Wake Resolution," AIAA Paper 2010-4554, June–July 2010.

[20] Wissink, A., Potsdam, M., Sankaran, V., Sitaraman, J., Yang, Z., and Mavriplis, D., "A Coupled Unstructured-Adaptive Cartesian CFD Approach for Hover Prediction," *Proceedings of the 66th Annual American Helicopter Society Forum*, Curran Associates, Inc., Red Hook, NY, 2010, pp. 2612–2629.

[21] Wissink, A., Jayaraman, B., Datta, A., Sitaraman, J., Potsdam, M., Kamkar, S., Mavriplis, D., Yang, Z., Jain, R., Lim, J., and Strawn, R., "Capability Enhancements in Version 3 of the Helios High-Fidelity Rotorcraft Simulation Code," AIAA Paper 2012-0713, Jan. 2012.

[22] Jung, M. S., and Kwon, O. J., "Numerical Simulation of Unsteady Rotor Flow Using an Unstructured Overset Mesh Flow Solver," *International Journal of Aeronautical and Space Sciences*, Vol. 10, No. 1, May 2009, pp. 104–111.
doi:10.5139/IJASS.2009.10.1.104

[23] Alauzet, F., and Olivier, G., "Extension of Metric-Based Anisotropic Mesh Adaptation to Time-Dependent Problems Involving Moving Geometries," AIAA Paper 2011-0896, Jan. 2011.

[24] Anderson, W. K., Rausch, R. D., and Bonhaus, D. L., "Implicit/Multigrid Algorithms for Incompressible Turbulent Flows on Unstructured Grids," *Journal of Computational Physics*, Vol. 128, No. 2, 1996, pp. 391–408.
doi:10.1006/jcph.1996.0219

[25] Chorin, A., "A Numerical Method for Solving Incompressible Viscous Flow Problems," *Journal of Computational Physics*, Vol. 135, No. 2, 1997, pp. 118–125.
doi:10.1006/jcph.1997.5716

[26] Vatsa, V. N., Carpenter, M. H., and Lockard, D. P., "Re-Evaluation of an Optimized Second Order Backward Difference (BDF2OPT) Scheme for Unsteady Flow Applications," AIAA Paper 2010-0122, Jan. 2010.

[27] Roe, P. L., "Approximate Riemann Solvers, Parameter Vectors, and Difference Schemes," *Journal of Computational Physics*, Vol. 43, No. 2, 1981, pp. 357–371.
doi:10.1016/0021-9991(81)90128-5

[28] Menter, F., "Two-Equation Eddy-Viscosity Turbulence Models for Engineering Applications," *AIAA Journal*, Vol. 32, No. 8, 1994, pp. 598–605.
doi:10.2514/3.12149

[29] Lynch, C. E., and Smith, M. J., "Hybrid RANS–LES Turbulence Models on Unstructured Grids," AIAA Paper 2008-3854, June 2008.

[30] Noack, R. W., Boger, D. A., Kunz, R. F., and Carrica, P. M., "Suggar++: An Improved General Overset Grid Assembly Capability," AIAA Paper 2009-3992, June 2009.

[31] Noack, R., "DiRTlib: A Library to Add an Overset Capability to Your Flow Solver," AIAA Paper 2005-5116, June 2005.

[32] Park, M. A., "Anisotropic Output-Based Adaptation with Tetrahedral Cut Cells for Compressible Flows," Ph.D. Thesis, Massachusetts Inst. of Technology, Cambridge, MA, 2008.

[33] Park, M., and Darmofal, D., "Parallel Anisotropic Tetrahedral Adaptation," AIAA Paper 2008-0917, Jan. 2008.

[34] Lee-Rausch, E., Park, M., Jones, W., Hammond, D., and Nielsen, E., "Application of Parallel Adjoint-Based Error Estimation and Anisotropic Grid Adaptation for Three-Dimensional Aerospace Configurations," AIAA Paper 2005-4842, June 2005.

[35] Jones, W., Nielsen, E., and Park, M., "Validation of 3D Adjoint-Based Error Estimation and Mesh Adaptation for Sonic Boom Predictions," AIAA Paper 2006-1150, Jan. 2006.

[36] Bibb, K., Gnoffo, P., Park, M., and Jones, W., "Parallel, Gradient-Based Anisotropic Mesh Adaptation for Re-Entry Vehicle Configurations," AIAA Paper 2006-3579, June 2006.

[37] Kamkar, S. J., "Mesh Adaptation Strategies for Vortex-Dominated Flows," Ph.D. Thesis, Stanford Univ., Stanford, CA, 2011.

[38] Venditti, D. A., "Grid Adaptation for Functional Outputs of Compressible Flow Simulations," Ph.D. Thesis, Massachusetts Inst. of Technology, Cambridge, MA, 2002.

[39] Brand, A. G., "An Experimental Investigation of the Interaction Between a Model Rotor and Airframe in Forward Flight," Ph.D. Thesis, Georgia Inst. of Technology, Atlanta, 1989.

[40] Mavris, D. N., "An Analytical Method for the Prediction of Unsteady Rotor/Airframe Interactions in Forward Flight," Ph.D. Thesis, Georgia Inst. of Technology, Atlanta, 1991.

[41] O'Brien, D. M. Jr., and Smith, M. J., "Analysis of Rotor–Fuselage Interactions Using Various Rotor Models," AIAA Paper 2005-0468, Jan. 2005.

[42] Lee, J., and Kwon, O. J., "Predicting Aerodynamic Fuselage Interactions by Using Unstructured Meshes," *Transactions of the Japan Society for Aeronautical and Space Sciences*, Vol. 44, No. 146, 2002, pp. 208–216.
doi:10.2322/tjsass.44.208

[43] Xu, H., and Ye, Z., "Euler Calculation of Rotor–Airframe Interaction Based on Unstructured Overset Grids," *Journal of Aircraft*, Vol. 48, No. 2, 2011, pp. 707–713.
doi:10.2514/1.C031051

[44] Sanchez-Rocha, M., Kirtas, M., and Menon, S., "Zonal Hybrid RANS–LES Method for Static and Oscillating Airfoils and Wings," AIAA Paper 2006-1256, Jan. 2006.

[45] Park, M. A., and Carlson, J., "Turbulent Output-Based Anisotropic Adaptation," AIAA Paper 2010-0168, Jan. 2010.